Inferring Shallow Surfaces on Sub-Neptune Exoplanets with JWST

Shang-Min Tsai[1] , Hamish Innes[1] , Tim Lichtenberg[1] , Jake Taylor[2] , Matej Malik[3] , Katy Chubb[4,5], and
Raymond Pierrehumbert[1]

[1] Atmospheric, Oceanic and Planetary Physics, Department of Physics, University of Oxford, UK
[2] Department of Physics and Institute for Research on Exoplanets, Université de Montréal, CA, USA
[3] Department of Astronomy, University of Maryland, College Park, USA
[4] Centre for Exoplanet Science, University of St. Andrews, North Haugh, St. Andrews, UK
[5] Stellar Astrophysics Centre, Department of Physics and Astronomy, Aarhus University, Ny Munkegade 120, Denmark

Abstract

Planets smaller than Neptune and larger than Earth make up the majority of the discovered exoplanets. Those with H_2-rich atmospheres are prime targets for atmospheric characterization. The transition between the two main classes, super-Earths and sub-Neptunes, is not clearly understood as the rocky surface is likely not accessible to observations. Tracking several trace gases (specifically the loss of ammonia (NH_3) and hydrogen cyanide (HCN)) has been proposed as a proxy for the presence of a shallow surface. In this work, we revisit the proposed mechanism of nitrogen conversion in detail and find its timescale on the order of a million years. NH_3 exhibits dual paths converting to N_2 or HCN, depending on the UV radiation of the star and the stage of the system. In addition, methanol (CH_3OH) is identified as a robust and complementary proxy for a shallow surface. We follow the fiducial example of K2-18b with a 2D photochemical model on an equatorial plane. We find a fairly uniform composition distribution below 0.1 mbar controlled by the dayside, as a result of slow chemical evolution. NH_3 and CH_3OH are concluded to be the most unambiguous proxies to infer surfaces on sub-Neptunes in the era of the James Webb Space Telescope.

Unified Astronomy Thesaurus concepts: Exoplanet atmospheres (487); Exoplanet atmospheric composition (2021); Exoplanets (498); Super Earths (1655); Mini Neptunes (1063)

Supporting material: tar.gz file

1. Introduction

Sub-Neptune-sized planets ($R_p \sim 1.6$–3.5 $R_\oplus$) constitute the main population of exoplanets we have discovered (Hsu et al. 2019). Yet their formation (Bean et al. 2021), atmospheric composition (Moses et al. 2013), and interior structure (Madhusudhan et al. 2020; Aguichine et al. 2021) are not well understood. A recurring question is whether these planets are close to scaled-up terrestrial planets or scaled-down ice giants. The mass–radius relation, when available, provides the first assessment. However, the bulk density can be highly degenerate from different mass fractions of the H_2/He envelope and iron/rocky core. Particularly the low-density (0.25 $\rho_\oplus$–0.75 $\rho_\oplus$) planets can either consist of a dense core enclosed by a massive H_2/He envelope or a lighter core (dominated by rocky material and/or water) with a shallow H_2-rich atmosphere.

Atmospheric observations provide potential diagnostics to distinguish the above two classes. Yu et al. (2021) suggest that atmospheric chemistry can be utilized to infer the pressure level of the atmosphere-interior interface. When the atmosphere is thin (e.g., <10 bar), photochemically unstable gases (e.g., ammonia (NH_3) and methane (CH_4)) would decline without being reformed through thermochemistry in the deep atmosphere. Hu et al. (2021) focus on the distinctive features of an ocean planet with a thin atmosphere where solubility equilibrium is expected. The temperate sub-Neptune K2-18b

with a recent water detection (Benneke et al. 2019; Tsiaras et al. 2019) is applied in both studies as a fiducial example. While Yu et al. (2021) do not consider atmosphere-surface exchanges, Hu et al. (2021) assume a plausible range of CO_2 concentrations in the initial atmosphere consistent with a massive water ocean. Nevertheless, both conclude that CH_4 in a 1 bar atmosphere is about 10–100 times less abundant than that in a massive atmosphere, independent of the amount of CO_2. Yu et al. (2021) show that the slow chemical recycling makes NH_3 the most sensitive species and a prominent proxy for the presence of surfaces. However, the amount of NH_3 in a 1 bar atmosphere predicted in both studies differs by orders of magnitude due to different assumptions of initial composition. Lastly, previous studies have commonly relied on 1D models and overlooked the interaction between dayside and nightside.

In this work, we first revisit the destruction mechanism driven by photochemistry that has been suggested to serve as an observational discriminator between shallow and deep atmospheres. We elucidate the timescale and duality of the nitrogen conversion with a quiet and an active M star, and for a range of atmospheric metallicity and vertical mixing. Finally, a key addition to previous work is that we apply a 2D model including day–night transport to reevaluate the viability of utilizing atmospheric chemistry as a proxy for the presence of surfaces.

2. Methods

2.1. 1D Radiative Transfer Model

To facilitate comparison with previous work, we take K2-18b as a test case for identifying the surface underneath a small

H$_2$ atmosphere. The pressure–temperature (P–T) profiles of K2-18b in dry radiative–convective equilibrium are computed by the radiative transfer model HELIOS (Malik et al. 2019a, 2019b). We assume a moderate 100 times solar metallicity (same as Yu et al. 2021) and an internal heat with $T_{int} = 30$ K (Lopez & Fortney 2013) with uniform heat redistribution. The P–T profile is not self-consistently evolving with chemistry but simply fixed as input to the photochemical model. We discuss the radiative effects of the surface in Section 3.1 and the radiative feedback of disequilibrium chemistry in Section 6.

2.2. 1D Photochemical Model

The atmospheric composition is computed using the photochemical kinetics model VULCAN (Tsai et al. 2017, 2021). The model treats photolysis, thermochemical kinetics, and vertical mixing. VULCAN has been applied to a variety of planetary atmospheres, including hot-Jupiters, sub-Neptunes, and Earth (e.g., Zilinskas et al. 2020; Tsai et al. 2021). We consider species containing N, C, O, and H for this study. The large-scale mixing process is parameterized by the eddy diffusion using the expression as a function of pressure in bar (P_{bar}) (Tsai et al. 2021) in our nominal model

$$K_{zz} = 10^5 \left(\frac{1\,\text{bar}}{P_{bar}} \right)^{0.4} \quad (\text{cm}^{2-1}). \qquad (1)$$

We further test the sensitive to eddy diffusion and the effects of surface sinks of ammonia, as discussed in Sections 3.5 and 6.

2.3. 2D Photochemical Model

The day–night circulation is expected to be crucial in regulating the compositional variation across a tidally locked planet (e.g., Agúndez et al. 2014; Drummond et al. 2020; Feng et al. 2020; Wardenier et al. 2021). We run the 2D photochemical model VULCAN on a pressure-longitude grid to account for the day–night transport on a meridionally averaged equatorial plane. The 2D model solves the continuity equations including horizontal transport

$$\frac{\partial n_i}{\partial t} = \mathcal{P}_i - \mathcal{L}_i - \frac{\partial \phi_{i,z}}{\partial z} - \frac{\partial \phi_{i,x}}{\partial x}, \qquad (2)$$

where n_i is the number density (cm^{-3}) of species i, $\mathcal{P}_i$ and $\mathcal{L}_i$ are the chemical production and loss rates (cm^{-3} s^{-1}) of species i, and $\phi_{i,z}$ and $\phi_{i,x}$ are the vertical and horizontal transport flux, respectively. The construction and benchmarks of 2D VULCAN are discussed in detail in a follow-up paper (in preparation). The 3D global circulation model (GCM) Exo-FMS with double gray radiation scheme is utilized to set up the input for the 2D photochemical model. Exo-FMS has previously been used in studies of both terrestrial exoplanet (Pierrehumbert & Ding 2016; Hammond & Pierrehumbert 2017, 2018; Pierrehumbert & Hammond 2019) and gas giant (Lee et al. 2020, 2021) atmospheres. The temperature and wind fields are averaged over the board equatorial zone across 45°, where the circulation is dominated by a zonal jet and well represented by a 2D framework. The equatorial region is then divided into four quarters by longitude: dayside (325°–45°), morning limb (45°–135°), nightside (135°–225°), and evening limb (225°–325°). The averaged zenith angles for the four

quarters are 32°, 72°, 0°, and 72°, respectively. The rms of the vertical wind velocity (w_{rms}) is converted to eddy diffusion by the mixing length theory $K_{zz} = w_{rms}H$, where H is the scale height as the characteristic length scale.

2.4. Transmission Spectrum Modeling

We use the radiative transfer and retrieval framework NEMESIS (Irwin et al. 2008) to produce the transmission spectra. The forward models were computed using the correlated-k technique, with the k-tables being computed using the methodology of Chubb et al. (2021). Specifically, the sources of the opacity data for the molecules of interest are NH$_3$ (Coles et al. 2019), CO (Li et al. 2015), CO$_2$ (Yurchenko et al. 2020), and CH$_3$OH[6] (Gordon et al. 2017).

3. 1D Results: Slow Loss of Ammonia

3.1. Minimal Surface Effects on the Thermal Structure

Before looking into the compositional diagnostics, we first discuss how the existence of surfaces might impact the thermal structure. The radiative effect of the surface is neglected in Yu et al. (2021) where the temperature profile is simply truncated at different pressure levels. In practice, the surface partially absorbs stellar irradiation and re-emits back to the atmosphere. A canonical example is that of Earth, where roughly half of the solar radiation is absorbed by the surface but the atmosphere is mostly opaque to infrared radiation. This potentially makes the temperature higher than that of a "surface-less" atmosphere at the same pressure level, which can in turn alter the composition and the ability to recycle atmospheric species.

We test the thermal effects of the surface using 1D radiative–convective calculations with a generic surface placed at different pressure levels. We assume a surface albedo of 0.1 but find no differences in the range of 0.1–0.3 (corresponding to the albedo range of land areas on Earth).[7] The resulting temperature profiles for 100 times solar metallicity are depicted in Figure 1. The convective zone extends from a few bar to 0.1 bar and the temperature is set by the dry adiabat. The presence of a surface turns out to have negligible thermal effects in this region since the atmosphere absorbs most of the stellar irradiation. Only for surface pressures around 0.01 bar, the greenhouse warming near the surface starts to be notable, because the atmosphere is optically thin toward stellar radiation while being thermally opaque in this region. In all cases, our test validates the approach of directly truncating the model for shallow atmospheres with surface pressure down to about 1 bar (also see May & Rauscher 2020 for the global heat transport).

3.2. Nitrogen Conversion for a Quiet M Star and an Active M Star

Photochemically active gases, including NH$_3$, HCN, and CH$_4$, are lost in the absence of a deep atmosphere where

---

[6] The opacity of CH$_3$OH is only available at room temperature but the temperature in the region sensitive to transmission ($P < 0.1$ bar) is also around 300 K.

[7] Note that we assume a wavelength-independent surface albedo, which likely underestimates the impact of the albedo on the surface temperature.
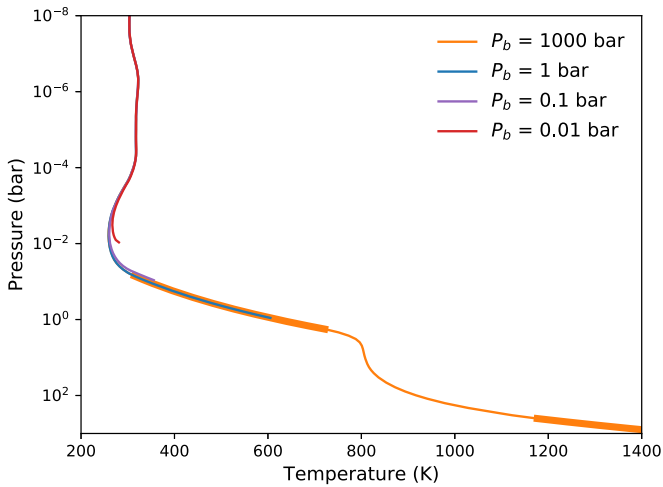
Figure 1. The pressure–temperature profiles of K2-18b with various surface pressure levels (P_b). Thickened lines indicate the convective regions. A solid surface appears to have minimal effect on the *P–T* profiles once the atmosphere is sufficiently opaque.

themochemistry operates fast and fully recycles them back. Comparing the results of a surface at 1 bar to the deep/ no-surface case, Yu et al. (2021) find that NH_3 is decreased by about 5 orders of magnitude while HCN is decreased by about 3 orders of magnitude. In this section, we will address the timescale of nitrogen conversion and overall compositional evolution driven by photochemistry. It is relevant to consider the host star at different stages when the timescale of chemical destruction is comparable to the timescale of stellar evolution. We apply the synthetic M2 star at the age of 45 Myr and 5 Gyr from HAZMAT (Peacock et al. 2020) for the stellar UV spectra, to represent a young, active and an old, quiet M star.[8]

Figure 2 shows snapshots of NH_3 and HCN abundances at different times with a 1 bar surface compared with a deep, 1000 bar surface, for both a quiet M star and an active M star.[9] All models start from initial abundances in chemical equilibrium. We first confirm that while recycling is enabled in the deep surface scenario, NH_3 and HCN settle to a steady state within 1000 yr. In the 1 bar atmosphere, NH_3 mostly drops off between 10 kyr and 1 Myr to a final mixing ratio several orders of magnitudes lower, qualitatively matching the decrease of NH_3 in Yu et al. (2021). However, as NH_3 is gradually lost, HCN does not readily follow NH_3. With a quiet M star, HCN actually increases to a uniform abundance close to 1% in the period between 0.1 and 10 Myr before gradually declining after 10 Myr.
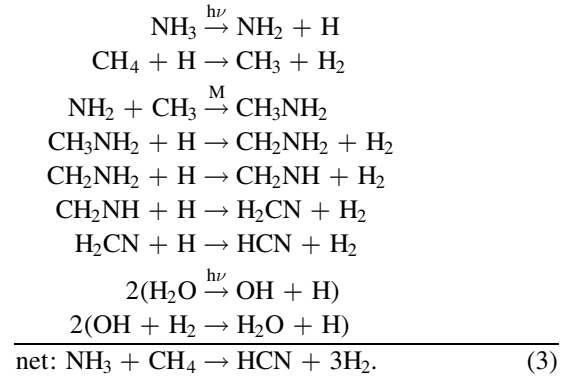
The timescale of nitrogen conversion given by the evolution of major nitrogen species is further captured in Figure 3(a). Overall, we find that nitrogen conversion takes place between 10 kyr and 1 Myr for an active M star and is much slower for a quiet M star. NH_3 is evidently converted to N_2 for an active M star, but HCN can serve as a transient nitrogen pool in the case of a quiet M star.

3.2.1. The Two Conversion Paths of NH₃

HCN is produced in the upper atmosphere initiated by NH_3 photolysis:

$$NH_3 \xrightarrow{h\nu} NH_2 + H$$
$$CH_4 + H \rightarrow CH_3 + H_2$$
$$NH_2 + CH_3 \xrightarrow{M} CH_3NH_2$$
$$CH_3NH_2 + H \rightarrow CH_2NH_2 + H_2$$
$$CH_2NH_2 + H \rightarrow CH_2NH + H_2$$
$$CH_2NH + H \rightarrow H_2CN + H_2$$
$$H_2CN + H \rightarrow HCN + H_2$$
$$2(H_2O \xrightarrow{h\nu} OH + H)$$
$$2(OH + H_2 \rightarrow H_2O + H)$$

net: $NH_3 + CH_4 \rightarrow HCN + 3H_2$. (3)

While HCN is subject to photodissociation into the cyanide radical (CN) and H, CN can rapidly recycle back to HCN with $CN + H_2 \rightarrow HCN + H$ in an H_2 atmosphere. In fact, the major effective sink of HCN is the OH radical produced by water photolysis. HCN is consumed by OH as C irreversibly goes into CO and N converted into N_2. The primary scheme for the loss of NH_3 and HCN through oxidation is

$$NH_3 \xrightarrow{h\nu} NH_2 + H$$
$$2(H_2O \xrightarrow{h\nu} OH + H)$$
$$CO + OH \rightarrow CO_2 + H$$
$$CO_2 \xrightarrow{h\nu} CO + O$$
$$HCN + OH \rightarrow HNCO + H$$
$$HNCO + H \rightarrow CO + NH_2$$
$$NH_2 + O \rightarrow HNO + H$$
$$HNO + H \rightarrow NO + H_2$$
$$2(H + H \xrightarrow{M} H_2)$$
$$NH_2 + NO \rightarrow N_2 + H_2O$$

net: $NH_3 + HCN + H_2O \rightarrow N_2 + CO + 3H_2$. (4)
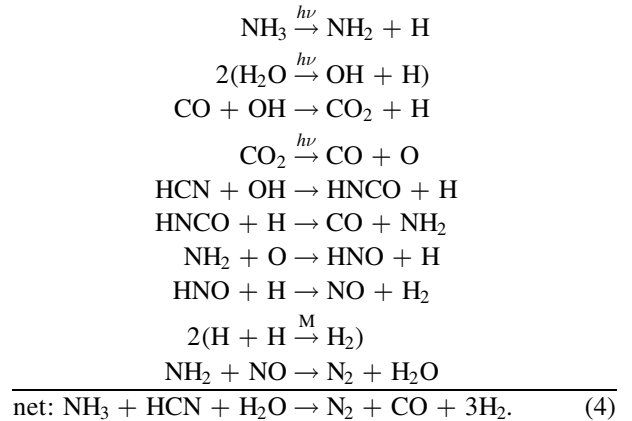
The critical difference between a quiet and an active M star is that an active M star produces orders of magnitude more OH radicals and hence HCN is scavenged more efficiently after building up. On the other hand, HCN is gradually consumed by OH only after 10 Myr with a quiet M star. We can estimate the overall nitrogen conversion timescale of scheme (4) with its rate-limiting step (Tsai et al. 2018)

$$\tau = \frac{[NH_3]}{k[NH_2][NO]},$$ (5)

where k is the rate coefficient for the reaction $NH_2 + NO \rightarrow N_2 + H_2O$. Taking the initial abundances at 0.1 mbar and 1000 yr, the timescale of NH_3 by (5) is ~0.1 Myr for an active M star and ~10 Gyr for a quiet M star, consistent with the kinetics results. This is not to be confused with the timescale of NH_3 photodissociation, which operates much faster, about a few hours at the same pressure level.

We conclude this section by reiterating that although the ammonia loss in the shallow-surface case is driven by photochemistry, the process of nitrogen conversion occurs
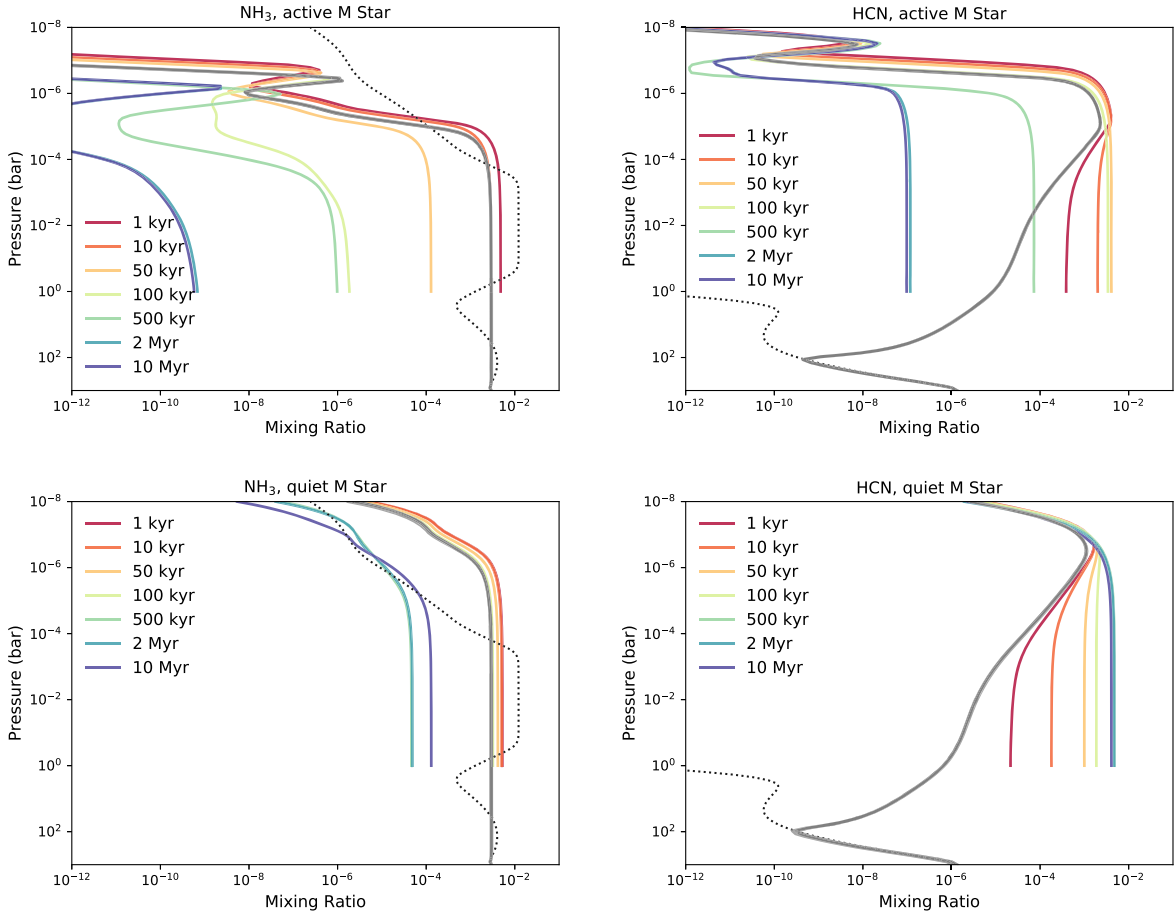
Figure 2. The evolution of the mixing ratio profiles of NH_3 (left) and HCN (right) with a 1 bar surface compared to a deep, 1000 bar atmosphere for an active (top) and a quiet (bottom) M star. The snapshot abundances at different times in the 1 bar surface model are color coded from red to blue. The abundances in the deep model do not evolve after 1 kyr because of the efficient thermochemistry in the deep atmosphere and are shown as solid gray lines. The black dotted curves indicate the initial equilibrium abundances. The upper panels are for an active M2 star at the age of 45 Myr and the lower panels for a quite M2 star at the age of 5 Gyr.

over a timescale of a million years or longer for quiet M stars. It resembles denitrification processes on a geological timescale but only takes place in the atmosphere rather than shifting between reservoirs.

3.3. Carbon Conversion

Most of the carbon is initially bound in the photochemically unstable CH_4 and converted into CO and CO_2 over time. The same evolution of carbon species is shown in Figures 3(b). First, carbon conversion takes about the same timescale as the nitrogen conversion, $\mathcal{O}$(Myr). Second, the conversion of CH_4 to CO and CO_2 is initiated by the CH_4 photodissociation channel: $CH_4 \overset{h\nu}{\rightarrow} CH + H_2 + H$. CH reacts with H_2O to form H_2CO, which is readily photodissociated into CO. This conversion proceeds faster with an active M star but the final abundances of CO and CO_2 remain close independent of the host star. Third, CH_4 is still continuously evolving after millions of years with a quiet M star, making it ambiguous to compare with the deep-atmosphere abundance as a proxy for surface pressure. Last and most interestingly, methanol (CH_3OH) is produced as a by-product of carbon conversion. A small part of H_2CO, instead of being photodissociated, can thermally react with hydrogen to form CH_3O and CH_3OH. The mixing ratio of CH_3OH is increased to $\sim 10^{-6}$, compared to $\lesssim 10^{-9}$ and $\lesssim 10^{-8}$ in the deep surface scenario for a quiet and

an active M star, respectively, where CH_3OH is transported and destroyed in the deep atmosphere.

3.4. Sensitivity to Metallicity

Sub-Neptunes can in general have a wide range of atmospheric metallicity (Moses et al. 2013; Fortney et al. 2013). The equilibrium abundance of NH_3 decreases with increasing metallicity as a result of hydrogen deficiency. To test the sensitivity of NH_3 conversion to metallicity, we further explore lower metallicities with the same P–T structure. Figure 3(c) illustrates the evolution of major nitrogen species for $1\times$, $10\times$, and $100\times$ solar metallicity, with a 1 bar surface and an active M star, where the abundances are normalized to those in equilibrium for a clearer comparison between different metallicities. The final $[NH_3]/[NH_3]_{EQ}$ slightly decreases with smaller metallicity while $[HCN]/[HCN]_{EQ}$ is almost identical for all metallicities. We find that the trends of NH_3 and HCN destruction remain robust. The $\mathcal{O}$(Myr) timescale of nitrogen conversion holds across different metallicities as well.

3.5. Sensitivity to Vertical Mixing

The eddy diffusion profile in our nominal model prescribed by Equation (1) is close to that in Yu et al. (2021). The inverse square root of pressure dependence of K_{zz} is commonly assumed to reflect the turbulent mixing due to gravity wave
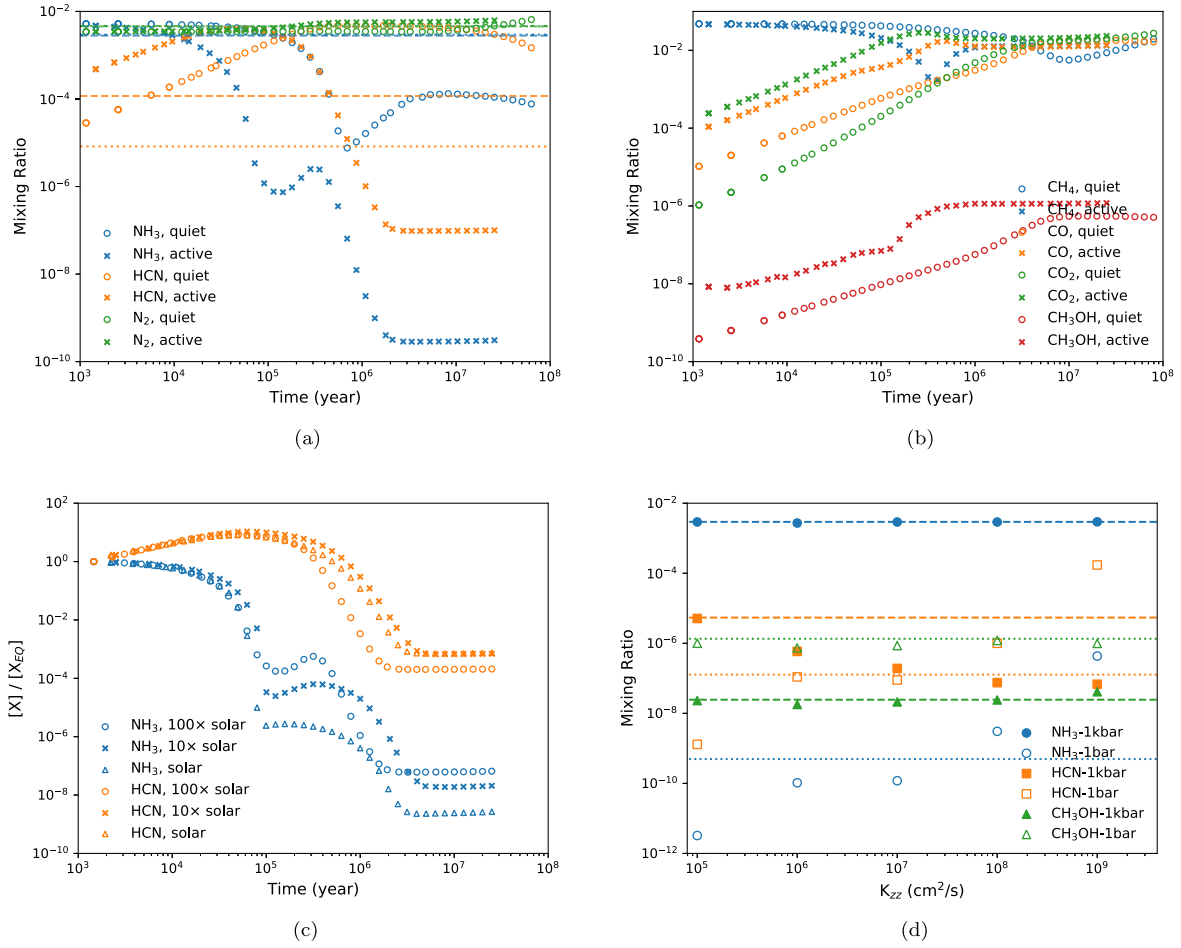
Figure 3. (a) The evolution of the column-averaged mixing ratios of NH_3 and HCN in an atmosphere with a 1 bar surface for a quiet and an active M star, where the dotted (quiet) and dashed (active) lines indicate the mixing ratios from the 1000 bar models for comparison. The column average is taken in the main observable part between 1 and 0.1 mbar where their volume mixing ratios are already close to uniform (Figure 2). (b) Same as (a) but for CH_4, CO, CO_2, and CH_3OH. (c) The evolution of the ratios between the abundances at a given time and their equilibrium abundances with an active M star for different atmospheric metallicities. (d) The final column-averaged mixing ratios of NH_3, HCN, and CH_3OH at 100 Myr with an active M star and a 1 bar surface (filled symbols) or 1000 bar surface (open symbols) for different values of uniform eddy diffusion. The dashed and dotted lines indicate the mixing ratios from the nominal 1000 bar and 1 bar models, respectively, where the eddy diffusion profile is given by Equation (1).

breaking in stratified atmospheres (e.g., Lindzen 1981; Moses et al. 2016). Since the eddy diffusion cannot be derived from first principles and is often treated as a free parameter, we further test the sensitivity to the strength and structure of vertical mixing by running the 1 bar surface case for a range of uniform K_{zz} profiles from 10^5 to 10^9 cm^2 s^{-1}. This range of eddy diffusion coefficient is consistent with that derived from the average vertical wind in the GCM of K2-18b (see Figure 8) and other sub-Neptunes in a similar dynamical regime (e.g., Charnay et al. 2015).

The mixing ratios of NH_3, HCN, and CH_3OH for different assumptions of eddy diffusion coefficient are reported in Figure 3(d). NH_3 in the deep model retains a uniform abundance (Figure 2) and does not depend on the eddy diffusion, whereas NH_3 decrease in the shallow model generally correlates with smaller eddy diffusion, since the lower well-mixed region leads to deeper UV penetration and photochemical destruction. Overall, NH_3 always has lower abundances in the shallow model than those in the deep model but the exact ratio, $[NH_3]_{1bar}/[NH_3]_{1kbar}$, depends on the strength and shape of K_{zz}. On the other hand, CH_3OH consistently shows little sensitivity to eddy diffusion and about two orders of magnitude increase with respect to the deep

model. Conversely, HCN highly depends on eddy diffusion as a result of the balance between photochemical production/ destruction in the upper atmosphere and vertical transport. HCN can either raise or lower in the presence of a shallow surface, making it unsuitable as a proxy for the surface level.

4. 2D Results: Globally Uniform Distribution Controlled by the Dayside

We have established the long, $\mathcal{O}$(Myr) timescale of the nitrogen conversion in Section 3. On a tidally locked exoplanet, the conversion driven by photochemistry only occurs on the dayside but completely shuts down on the permanent nightside. Without photolysis, NH_3 is able to maintain a high abundance on the nightside. To answer the question of how the chemical evolution with a shallow surface would be regulated by the global circulation between the dayside and nightside, we apply a 2D photochemical model on a meridionally averaged equatorial plane to address the effects of day–night transport.

The temperature and wind for the 2D photochemical model are adopted from the 3D GCM output of K2-18b, whose global structure can be found in Figure 8. We employ four quarters (Figure 8(d)) in our 2D model for clarity, while the full 2D
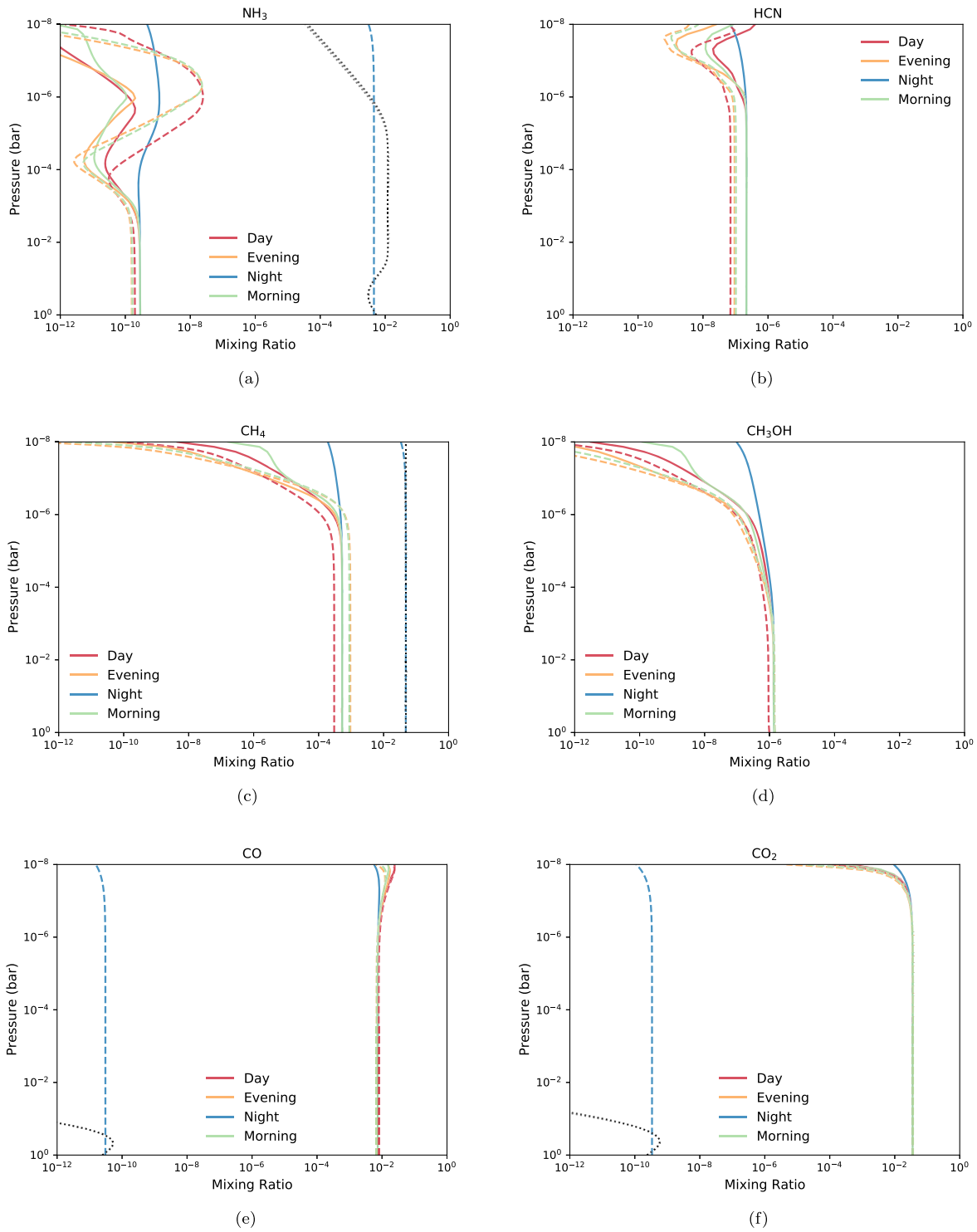
Figure 4. The final mixing ratios of several species that can be potential surface indicators in the four quarters for an active M star, comparing simulations with (solid) and without (dashed) zonal wind. The black dotted lines indicate the equilibrium composition, which follows the global temperature.

chemical output is included in the supplementary figure. To isolate the effects of horizontal transport, Figure 4 compares the steady-state abundances with a 1 bar surface and an active M star to those without including the zonal wind with the averaged temperature, zonal wind, and inferred eddy diffusion profiles for the four quarters summarized in panel (d) included in Figure 6.

It is evident that without a recycling mechanism, the horizontal transport is able to exhaust NH_3 on the nightside.

Even the modest zonal wind ($\sim 1 \, \mathrm{m \, s^{-1}}$) yields a horizontal transport timescale of less than a year, orders of magnitude faster than the chemical evolution. As a result, most species are homogenized below 1 mbar and exhibit abundances close to those predicted by the 1D model without day–night transport. The model for a quiet M star shows qualitatively consistent results (Figure 7), with reduced photochemical destruction of NH_3 and higher abundance of HCN. The results we find for the fiducial example of K2-18b can be generalized to most

temperate, tidally locked planets with a chemically inactive surface, since the equatorial jet is a robust dynamical property (e.g., Pierrehumbert & Hammond 2019).

5. Spectral Indicator

Since the 1D model for the dayside is verified to represent the globally uniform distribution, we compare the transmission spectra from our deep-atmosphere and shallow-surface models in Figure 5. The most distinctive differences are CO_2 absorption features at 4.2–5 μm and the lack of NH_3 at 3, 8.8–12 μm for the shallow-surface case. Interestingly, CH_3OH absorbs between 9 and 10 μm, well within the NH_3 band. To quantify the ability of detecting these molecules with JWST, we used Pandexo (Batalha et al. 2017) to generate the required observations to disentangle between our two models. We find that with it is possible to identify the NH_3 feature at 3 μm with only three transit observations using NIRSpec. When observing with MIRI, it is possible to further discriminate CH_3OH from NH_3 with around 20 transits. Conversely, HCN is not abundant enough in the region sensitive to transmission to show observable features.

6. Discussion

Interactions with the planetary interior are not included in this work as we assume zero flux at the lower (surface) boundary for all species. Regarding NH_3, agricultural ammonia on Earth is absorbed by surfaces with a fairly short residence time ($\sim$days, e.g., Jia et al. 2016; Seinfeld & Pandis 2016). We have tested our model with Earth surface conditions assuming biotic processes are involved, and even the slowest dry deposition of NH_3 on a desert ($v_{dep} = 0.0002\,cms^{-1}$, Jia et al. 2016) acts as a more efficient sink than the photochemical sink (Section 3). However, without the biosphere transferring ammonia to different organic nitrogen, it is conceivable that ammonia returns to the atmosphere at once and makes effectively net zero deposition. In general, various geological processes can be crucial in controlling trace gases in the atmosphere, especially determining the redox state of the atmosphere. For example, Wogan et al. (2020) find volcanic outgassing unlikely to be reducing, while Lichtenberg (2021) demonstrate that the interior of sub-Neptunes can remain reducing due to vigorous internal convection and Zahnle et al. (2020) suggest iron-rich impacts can also generate reducing atmospheres that favor NH_3 and CH_4. In the case of an atmosphere with scattering clouds/hazes or less irradiated than K2-18b (Piette & Madhusudhan 2020; Blain et al. 2021), the surface temperature can be brought down to suppress water evaporation (Scheucher et al. 2020) and allow liquid water oceans, which can participate in regulating the inventory of soluble gases (e.g., NH_3, CO_2, and CH_3OH). With mobile lid tectonics (Tackley et al. 2013; Meier et al. 2021), the long-term evolution of CO_2 in the shallow atmosphere case is expected to be governed by outgassing and weathering (e.g., Pierrehumbert 2010).

Since CO_2 generally has other geological sources and HCN is unsuitable as a surface proxy for its strong dependence on the stellar type and vertical mixing, we propose including CH_3OH as a complementary indicator along with NH_3. On Earth,
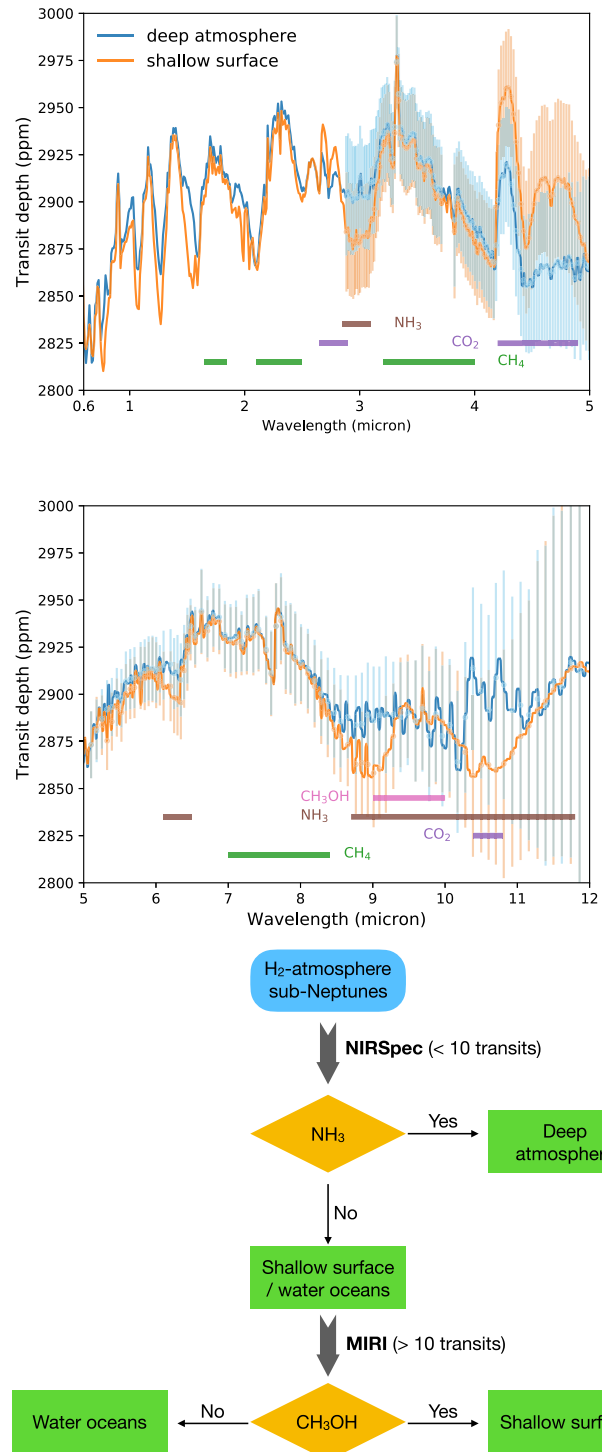

Figure 5. The synthetic transmission spectra of K2-18b (top and middle panels) for the deep (1000 bar boundary; shown in blue) and shallow (1 bar surface; shown in orange) model. Points with error bars (light blue: deep atmosphere; light orange: 1 bar surface) are simulated observations by the JWST NIRSpec G395H for three transits (top) and MIRI LRS for 20 transits (middle) without scatter produced by Pandexo (Batalha et al. 2017). The absorption features of several molecules are indicated by the color bands. The bottom panel shows the flowchart to progressively identify shallow surfaces and ocean worlds with JWST instruments.
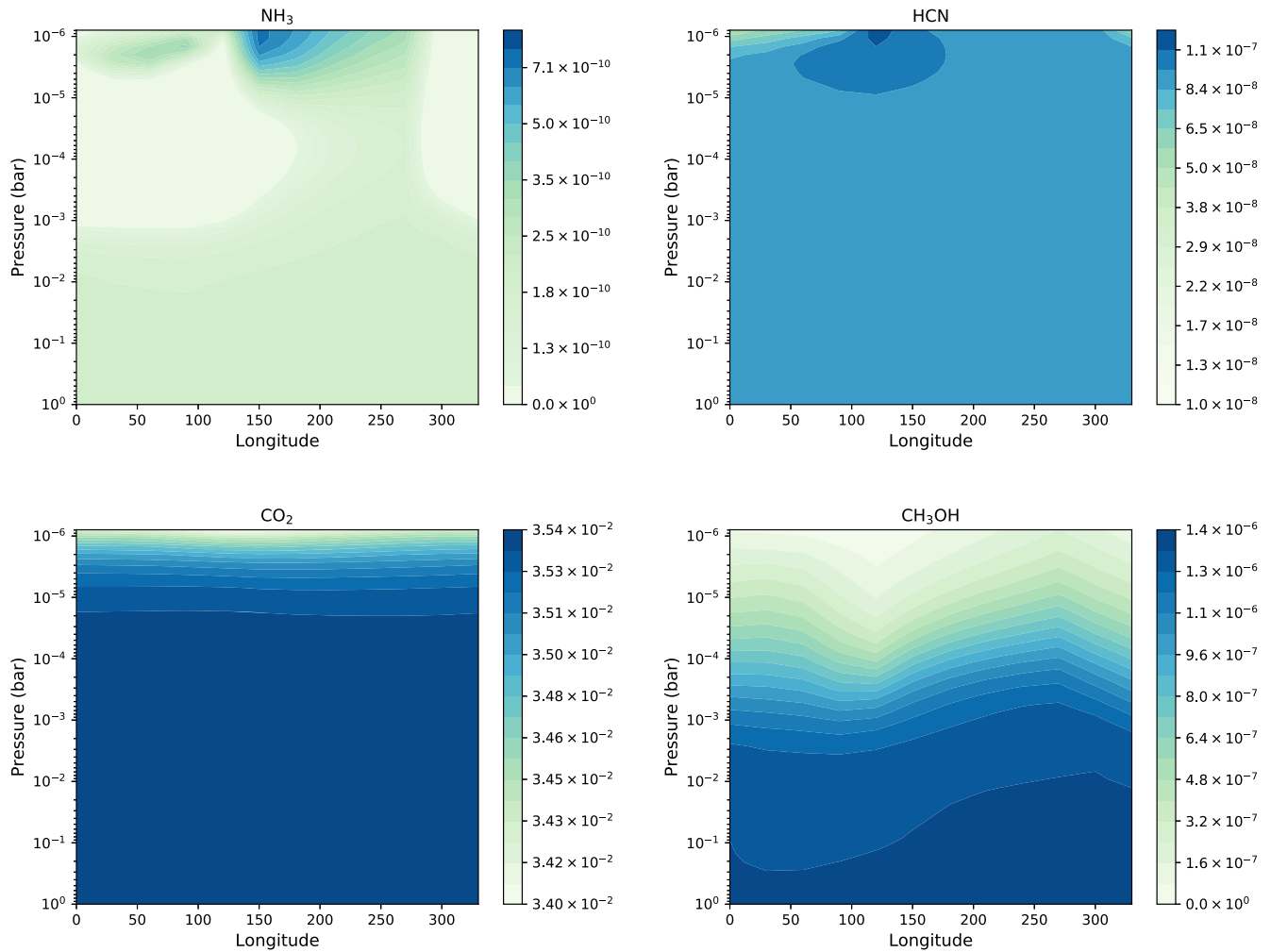
Figure 6. Full distribution of NH_3, HCN, CO, and CO_2 as a function of longitude (substellar point at $0°$) and pressure on the meridionally averaged equatorial plane of K2-18b with an active M star, computed with the 2D photochemical model.

CH_3OH is mainly produced by plants and deposited to the ocean (Yang et al. 2013), whereas in a H_2-dominated atmosphere with a shallow surface, CH_3OH is produced during the process of CH_4 oxidation. Detection of NH_3 without CH_3OH is consistent with the deep/no-surface scenario, while detection of CH_3OH but without NH_3 indicates the presence of a surface. Nondetection of both NH_3 and CH_3OH can imply a global water-ocean world (Hu et al. 2021) as they are highly soluble in water. We summarize the flowchart of inferring the surface property of sub-Neptunes with H_2-dominated atmospheres using JWST in the bottom panel of Figure 5.

surface. Instead, the shallow-surface scenario can be ruled out by NH_3 detection, whereas positive detection of CH_3OH with negative detection of NH_3 indicate shallow and dry surfaces.

7. Summary

1D modeling of sub-Neptune exoplanets suggests that NH_3 is depleted below a detectable level on the dayside in the presence of a shallow surface, while HCN can either increase or decrease depending on vertical mixing and quiet/active M stars. CH_3OH is found to be consistently enhanced for all shallow-surface simulations. We construct a 2D photochemical framework to account for the day–night circulation and find the global abundance is overall quenched from the dayside as the chemical conversion takes $\mathcal{O}(\mathrm{Myr})$. Our results suggest that HCN is not applicable to determine the pressure level of the

Appendix A
Radiative Feedback from Disequilibrium Chemistry

Since the temperature structure is fixed by thermochemical equilibrium, we have also checked the radiative feedback as a result of disequilibrium chemistry. We rerun the 1D radiative–convective calculations with the final disequilibrium composition from Section 3. We find the resulting temperature from disequilibrium chemistry can be about 100 K lower at most in the convective zone above 1 bar, mainly from the decrease of opacity-predominating water. We have performed sensitivity tests and found the temperature difference does not alter the presented results (also see
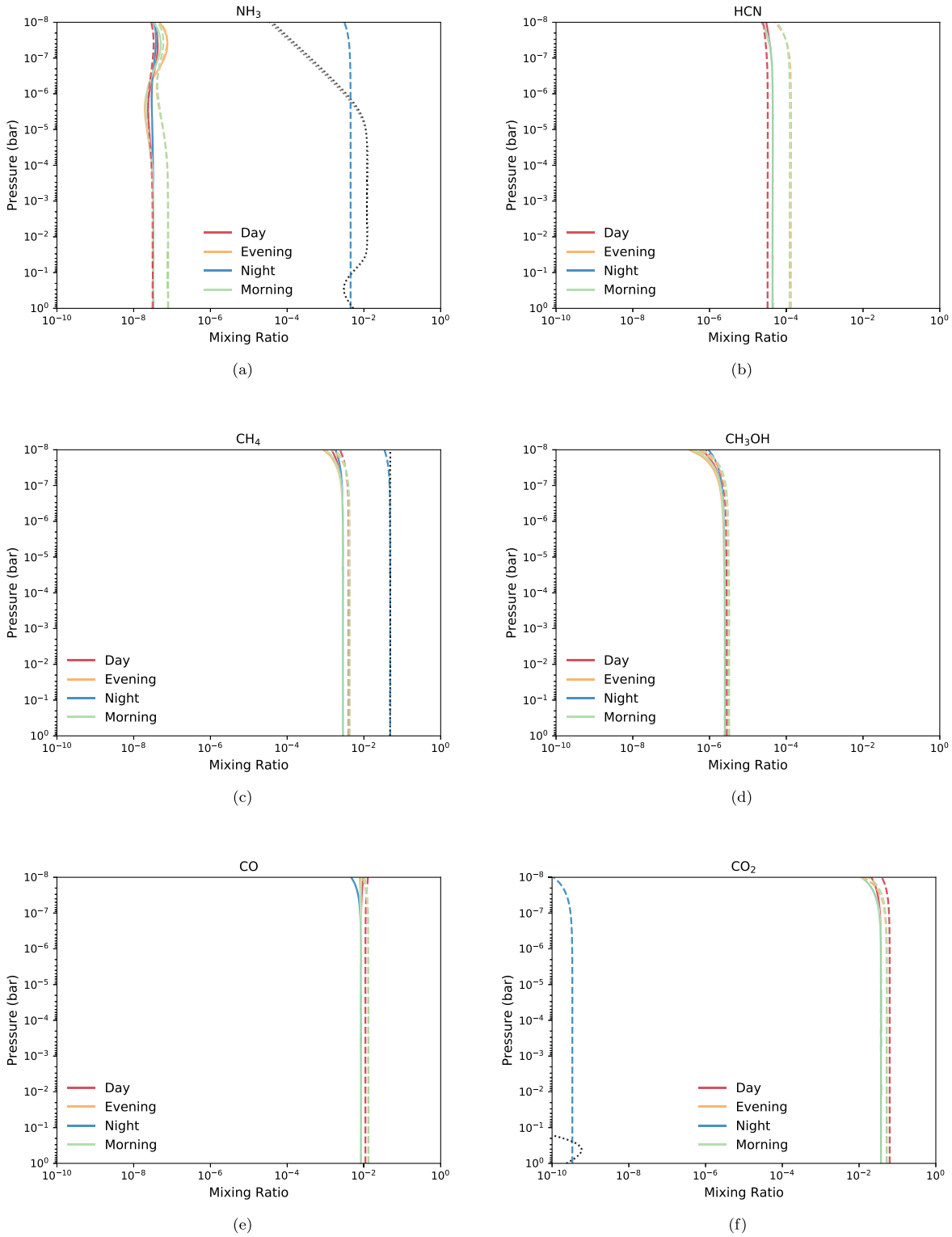
Figure 7. Same as Figures 4(a)–(f) except for a quiet M star.

the thermal structure variance explored in Yu et al. 2021). We will leave the effects of water condensation for future work.

Appendix B
Running 2D Photochemical Models for Millions Years

The horizontal transport flux by the zonal wind in Equation (2) yields a hyperbolic partial differential equation.

The time step is ought to follow the same format as the Courant–Friedrichs–Lewy condition when numerically integrating the system. In other words, the time step must not exceed the time that zonal flow travels across adjacent vertical columns. For K2-18b, the time step limit is $\frac{\Delta x}{u} \sim 10^5$ s, which means more than 10^8 integration steps are required to integrate the system to a million years for the long-term chemical
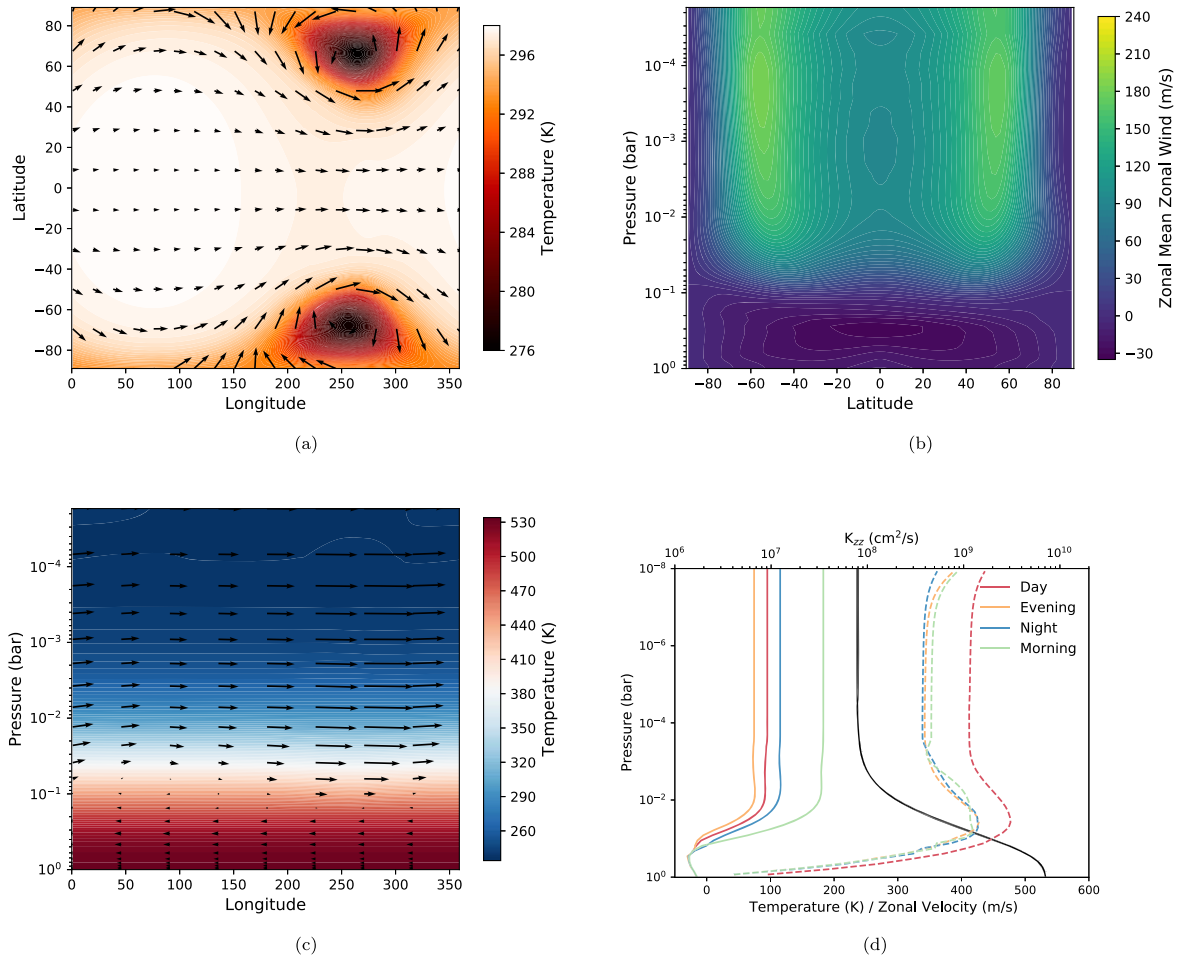
Figure 8. The 3D general circulation output of K2-18b with a 1 bar rocky surface, with all quantities averaged over the last 1000 (Earth) days of the 10000 day simulation. Panel (a) shows the temperature (color scale) and horizontal wind (arrows) at 9.7 mbar level. Panel (b) shows the zonal-mean zonal wind. Panel (c) visualizes the temperature (color scale) and wind on the meridionally averaged equatorial plane, with the substellar point at 0° longitude. Panel (d) summarizes the averaged (explained in Section 2.3) temperature (black), zonal wind (solid), and eddy diffusion profiles (dashed) for the four quarters of K2-18b. All temperature profiles are represented by black lines and overlap because the temperature is globally uniform, whereas the zonal wind and eddy diffusion (derived from the vertical wind) profiles are color coded for the dayside, evening, nightside, and morning quarter.

evolution. To circumvent this computational load, we arbitrarily slow down the zonal wind (e.g., by 1000 times) such that a larger time step can be adopted. Once the chemistry has evolved after the megayear integration, we recover the correct wind velocity and run the model to final steady state. This seemingly risky approach can be justified by the timescale argument—the horizontal transport effectively interacts with vertical mixing and chemical evolution, which manifest drastically different timescales. The timescale of vertical mixing is within hours and the chemical evolution takes $\mathcal{O}(\mathrm{Myr})$, whereas the nominal horizontal transport has a timescale of ~days. Therefore, the long-term compositional evolution is expected to be qualitatively unaffected for any horizontal transport much slower than vertical mixing but orders of magnitude faster than the chemical evolution. That is, the tuned-down zonal wind still plays the role of passing on the chemical evolution from dayside to nightside. Finally, we have confirmed this approach by comparing the simulation at about 5000 yr to that with 1000 times slower zonal wind and found no differences.

ORCID iDs

Shang-Min Tsai https://orcid.org/0000-0002-8163-4608
Hamish Innes https://orcid.org/0000-0001-5271-0635
Tim Lichtenberg https://orcid.org/0000-0002-3286-7683
Jake Taylor https://orcid.org/0000-0003-4844-9838
Matej Malik https://orcid.org/0000-0002-2110-6694
Raymond Pierrehumbert https://orcid.org/0000-0002-5887-1197

References

Aguichine, A., Mousis, O., Deleuil, M., & Marcq, E. 2021, ApJ, 914, 84
Agúndez, M., Venot, O., Selsis, F., & Iro, N. 2014, ApJ, 781, 68
Batalha, N. E., Mandell, A., Pontoppidan, K., et al. 2017, PASP, 129, 064501
Bean, J. L., Raymond, S. N., & Owen, J. E. 2021, JGRE, 126, e06639
Benneke, B., Wong, I., Piaulet, C., et al. 2019, ApJL, 887, L14
Blain, D., Charnay, B., & Bézard, B. 2021, A&A, 646, A15
Charnay, B., Meadows, V., & Leconte, J. 2015, ApJ, 813, 15
Chubb, K. L., Rocchetto, M., Yurchenko, S. N., et al. 2021, A&A, 646, A21
Coles, P. A., Yurchenko, S. N., & Tennyson, J. 2019, MNRAS, 490, 4638
Drummond, B., Hébrard, E., Mayne, N. J., et al. 2020, A&A, 636, A68
Feng, Y. K., Line, M. R., & Fortney, J. J. 2020, AJ, 160, 137

Fortney, J. J., Mordasini, C., Nettelmann, N., et al. 2013, ApJ, 775, 80
Gordon, I. E., Rothman, L. S, Hill, C., et al. 2017, JQSRT, 203, 3
Hammond, M., & Pierrehumbert, R. T. 2017, ApJ, 849, 152
Hammond, M., & Pierrehumbert, R. T. 2018, ApJ, 869, 65
Hsu, D. C., Ford, E. B., Ragozzine, D., & Ashby, K. 2019, AJ, 158, 109
Hu, R., Damiano, M., Scheucher, M., et al. 2021, https://doi.org/10.21203/rs.3.rs-481864/v1
Irwin, P. G. J., Teanby, N. A., de Kok, R., et al. 2008, JQSRT, 109, 1136
Jia, Y., Yu, G., Gao, Y., et al. 2016, NatSR, 6, 19810
Lee, E. K. H., Parmentier, V., Hammond, M., et al. 2021, MNRAS, 506, 2695
Lee, G. K., Casewell, S. L., Chubb, K. L., et al. 2020, MNRAS, 496, 4674
Li, G., Gordon, I. E., Rothman, L. S., et al. 2015, ApJS, 216, 15
Lichtenberg, T. 2021, ApJL, 914, L4
Lindzen, R. S. 1981, JGRC, 86, 9707
Lopez, E. D., & Fortney, J. J. 2013, ApJ, 776, 2
Madhusudhan, N., Nixon, M. C., Welbanks, L., Piette, A. A. A., & Booth, R. A. 2020, ApJL, 891, L7
Malik, M., Kempton, E. M. R., Koll, D. D. B., et al. 2019b, ApJ, 886, 142
Malik, M., Kitzmann, D., Mendonça, J. M., et al. 2019a, AJ, 157, 170
May, E. M., & Rauscher, E. 2020, ApJ, 893, 161
Meier, T. G., Bower, D. J., Lichtenberg, T., Tackley, P. J., & Demory, B.-O. 2021, ApJL, 908, L48
Moses, J. I., Line, M. R., Visscher, C., et al. 2013, ApJ, 777, 34
Moses, J. I., Marley, M. S., Zahnle, K., et al. 2016, ApJ, 829, 66
Peacock, S., Barman, T., Shkolnik, E. L., et al. 2020, ApJ, 895, 5
Pierrehumbert, R. T. 2010, Principles of Planetary Climate (Cambridge: Cambridge Univ. Press)
Pierrehumbert, R. T., & Ding, F. 2016, RSPSA, 472, 20160107
Pierrehumbert, R. T., & Hammond, M. 2019, AnRFM, 51, 275
Piette, A. A. A., & Madhusudhan, N. 2020, ApJ, 904, 154
Scheucher, M., Wunderlich, F., Grenfell, J. L., et al. 2020, ApJ, 898, 44
Seinfeld, J. H., & Pandis, S. N. 2016, Atmospheric Chemistry and Physics: From Air Pollution to Climate Change (New York: Wiley)
Tackley, P. J., Ammann, M., Brodholt, J. P., Dobson, D. P., & Valencia, D. 2013, Icar, 225, 50
Tsai, S.-M., Kitzmann, D., Lyons, J. R., et al. 2018, ApJ, 862, 31
Tsai, S.-M., Lyons, J. R., Grosheintz, L., et al. 2017, ApJS, 228, 20
Tsai, S.-M., Malik, M., Kitzmann, D., et al. 2021, arXiv:2108.01790
Tsiaras, A., Waldmann, I. P., Tinetti, G., Tennyson, J., & Yurchenko, S. N. 2019, NatAs, 3, 1086
Wardenier, J. P., Parmentier, V., Lee, E. K. H., Line, M. R., & Gharib-Nezhad, E. 2021, MNRAS, 506, 1258
Wogan, N., Krissansen-Totton, J., & Catling, D. C. 2020, PSJ, 1, 58
Yang, M., Nightingale, P. D., Beale, R., et al. 2013, PNAS, 110, 20034
Yu, X., Moses, J. I., Fortney, J. J., & Zhang, X. 2021, ApJ, 914, 38
Yurchenko, S. N., Mellor, T. M., Freedman, R. S., & Tennyson, J. 2020, MNRAS, 496, 5282
Zahnle, K. J., Lupu, R., Catling, D. C., & Wogan, N. 2020, PSJ, 1, 11
Zilinskas, M., Miguel, Y., Mollière, P., & Tsai, S.-M. 2020, MNRAS, 494, 1490